JOURNAL OF THEORETICAL
AND APPLIED MECHANICS
3, **40**, 2002

OPTOPIEZOTHERMOELASTIC ACTIONS AND MICRO-CONTROL SENSITIVITY ANALYSIS OF CYLINDRICAL OPTO-MECHANICAL SHELL ACTUATORS

HORN-SEN TZOU

Department of Mechanical Engineering, StrucTronics Laboratory University of Kentucky, USA
e-mail: hstzou@engr.uky.edu

BAO-JIANG LIU

Department of Mechanical Engineering, University of Waterloo, Waterloo, Canada

DAVID CSELEDY

Lexmark, Lexington, KY

Opto-mechanical actuators controlled by high-energy lights represent a new class of non-contact precision actuators based on the photodeformation process. The photodeformation process involves two fundamental opto-piezo(electric)thermoelastic coupling phenomena: 1) the photovoltaic effect and 2) the converse piezoelectric effect. Irradiating high-energy lights, such as lasers or ultraviolet lights, on a certain class of photostrictive materials can trigger the photodeformation and, consequently the induced photodeformation can be used for non-contact precision actuation and control. In the process of photodeformation, the temperature induced pyroelectric effect and the thermal strain effect also affect the overall response. This paper is to evaluate the micro-actuation sensitivity and spatial effectiveness of distributed opto-mechanical shell actuators. Mathematical modeling of a circular cylinder laminated with a segmented opto-mechanical actuator patch is presented first, followed by analytical solution procedures. Various design parameters and micro-control actions, e.g., membrane control, bending control, actuator location, actuator length/size, are evaluated and their modal control sensitivities are reported. Time histories of free and controlled responses are demonstrated.

Key words: photodeformation, photovoltaic effect, converse effect, pyroelectric effect

1. Introduction

Conventional structural and mechanical systems are usually divided into two major categories: 1) the discrete (or lumped) system and 2) the distributed

(or continuous) system. Dynamic responses of discrete systems are functions of time, and those of distributed systems are functions of time and space (spatial variables). Furthermore, control of distributed systems can be achieved using either discrete or distributed actuators. Discrete devices applied to control of distributed systems are extremely sensitive to their spatial locations. They are virtually useless if located at modal nodes or lines. On the other hand, distributed actuators are more effective to control of distributed systems (Tzou and Bergman, 1998).

Shells and shell-type structures are widely used in many advanced engineering applications, ranging from micro-nozzles to aerospace structures (e.g., antennas, solar panels, etc.). There are two essential control techniques used to accomplish distributed control of shells, i.e., 1) the passive technique and 2) the active technique. The passive technique usually involves energy absorption and dissipation devices, e.g., viscoelastic dampers, dynamic absorbers, constraint-layer dampers, etc. The active control technique, however, usually utilizes actuators and/or counteracting devices, e.g., electromechanical actuators, piezoelectric actuators, proof-mass dampers, active constraint-layer dampers, etc. (Tzou and Fukuda, 1992). This paper focuses on the distributed control of distributed systems (i.e., continua – shells and plates) using active non-contact distributed opto-mechanical actuators.

Conventional actuators require hard-wire connections to transmit energy sources and control commands to activate the actuator mechanisms. The hard-wire signal transmission busses can easily attract undesirable electric noises influenced by electrical and/or magnetic fields, long distance transmissions, etc. Accordingly, noises and uncertainties are often involved and control commands may not be accurately executed. In this study, non-contact distributed opto-mechanical actuators activated by high-energy lights are investigated and their microscopic distributed control characteristics are evaluated. Light driven opto-mechanical actuators have many advantages over conventional hard-wired electromechanical actuators, such as 1) non-contact actuation, 2) immune from electric/magnetic disturbances, 3) compact and lightweight, etc. Brody (1983), Suski et al. (1990), Morikawa et al. (1993), and Fukuda et al. (1993) studied one-dimensional (beam-type) opto-mechanical actuators. Piezothermoelastic coupling of precision piezoelectric systems was investigated (Tzou and Ye, 1994). Two-dimensional planar (plate-type) opto-mechanical actuators with applications to distributed vibration control were investigated (Liu and Tzou, 1996; 1998; Shih and Tzou, 2000). An opto-mechanical multi-degree-of-freedom actuator was also proposed and its performance evaluated (Tzou and Chou, 1996). Distributed opto-mechanical shell actuators

and their control effectiveness were initially evaluated (Tzou and Liu, 1997). This paper is concerned with the micro-control sensitivity analysis of distributed opto-mechanical shell actuators laminated on cylindrical shells. Sensing and control sensitivities with respect to geometry and location variations are studied. Micro-control actions and shell control effectiveness with respect to common design variables (such as locations, length, width, etc.) are evaluated.

2. Micro-photodeformation induced control actions

High-energy lights, e.g., lasers, ultraviolet lights, etc., irradiated on distributed opto-mechanical actuators induces a photodeformation process. Figure 1 illustrates the opto-piezo(electric)thermoelastic coupling of the photodeformation process. Detailed microscopic opto-piezothermoelastic characteristics and control actions are discussed in this section.

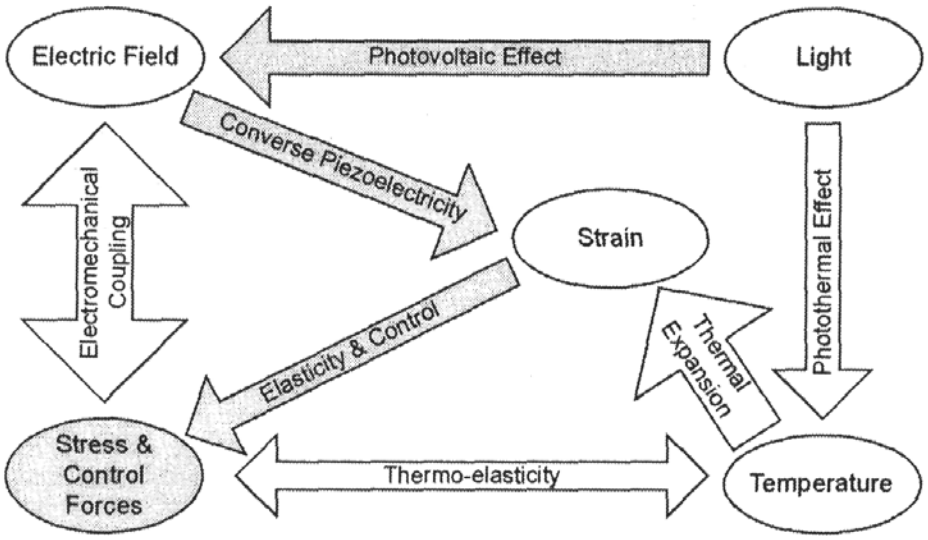

Fig. 1. Photo-piezoelectric-thermoelastic coupling

The photodeformation process involves two fundamental effects: 1) the photovoltaic effect and 2) the converse piezoelectric effect – i.e., the shaded path in Figure 1. The light irradiated on the optical actuator first induces a charge flowing, opposite to the polarized direction, usually from the lighted surface to the dark surface. This charge flow causes a voltage generation between the surface electrodes. This process is called the photovoltaic effect. This voltage consequently induces mechanical strains due to the converse piezoelectric effect. In addition, the high-energy light also heats up the opto-mechanical

actuator, and the temperature change triggers the pyroelectric effect from which a secondary pyroelectric voltage further enhances the strain generation due to the converse effect. For an opto-electromechanical actuator irradiated by the high-intensity light $I(t_j)$, the induced in-plane electric field $E_I^o(t_j)$ and the body temperature $\theta(t_j)$ at the time instant t_j are defined as

$$\begin{aligned} E_I^o(t_j) &= E_I^o(t_{j-1}) + [E_s^o - E_I^o(t_{j-1})]\alpha_o I(t_j)\mathrm{e}^{-\alpha_o I(t_j)\Delta t}\Delta t - \\ &\quad -E_I^o(t_{j-1})\beta_o \mathrm{e}^{-\beta_o \Delta t}\Delta t \\ \theta(t_j) &= \theta(t_{j-1}) + \frac{1}{H + \gamma_o \Delta t}[I(t_j)W - \gamma_o \theta(t_{j-1})\Delta t] \end{aligned} \tag{2.1}$$

where E_s^o is the saturation voltage; $\alpha_o = \alpha/a_s$ (α is the opto-mechanical actuator constant and $a_s = a/b$ (length/width) is the aspect ratio); β_o is the voltage leakage constant; γ_o is the heat transfer rate; W is the power of absorbed heat; H is the heat capacity; and Δt is the time step. Note that properties associated with the opto-mechanical actuator are denoted by either a subscript or a superscript o and light-related parameters/variables are denoted by a subscript I in notations. As noted earlier, the heat can trigger the pyroelectric effect from which an additional voltage is generated. The electric field $E_\theta^o(t)$, contributed by the pyroelectric effect, can be determined from

$$E_\theta^o(t) = \frac{p_o}{\varepsilon_o}\theta(t) \tag{2.2}$$

where p_o is the pyroelectric constant; ε_o is the permittivity; the subscript θ denotes the temperature. Accordingly, the total induced electric field $E_{I\theta}^o(t)$ including both the photovoltaic effect and the pyroelectric effect is

$$E_{I\theta}^o(t) = E_I^o(t) + E_\theta^o(t) \tag{2.3}$$

Furthermore, there are two temperature induced strain components. One is due to the thermal strain effect and the other is due to the pyroelectric effect. The photovoltaic effect and the pyroelectric effect can induce a positive strain. Since heat interferes with the photostriction, the thermal effect introduces a negative strain of the material (Fukuda et al., 1993). Thus, the total magnitude of the light induced photodeformation and the strains $S_{ij}(t)$ can be expressed as

$$S_{ij}(t) = d_{3i}E_{I\theta}^o(t) + \frac{1}{Y_p^o}\lambda_I \theta(t) \tag{2.4}$$

where d_{3i} is the piezoelectric-strain constant, λ_I is a thermal stress coefficient, and Y_p^o is Young's modulus of the opto-mechanical actuator. The actuator

strain is along its polarization direction and the corresponding stress – the micro-control action – can be used in precision control. With appropriate layouts and configurations, this photodeformation induced strain can introduce control forces and moments and ultimately apply to non-contact precision manipulation and control of structronic and mechatronic systems. Note that these fundamental opto-piezothermoelastic equations will be further elaborated and incorporated into control of cylindrical shells discussed later.

3. Distributed vibration control of cylindrical shells

Modeling of a simply supported circular cylindrical shell, with the radius R, length L and thickness h, laminated with a distributed opto-mechanical actuator patch is studied and its control effects are evaluated in this section. The cylindrical shell is defined in a cylindrical coordinate system, i.e., $\alpha_1 = x$, $\alpha_2 = \beta$, and α_3, see Figure 2.

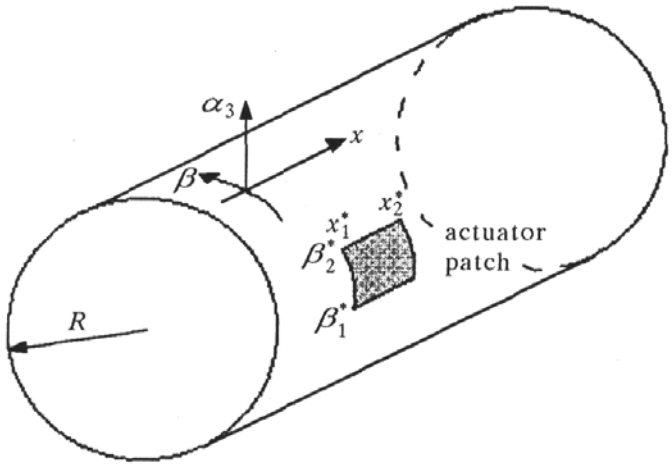

Fig. 2. A circular cylindrical shell tube with an opto-mechanical actuator patch

A generic opto-mechancial actuator patch covers a part of the cylinder defined by the coordinates x_1^* to x_2^* and β_1^* to β_2^*. The system equations in the three axial directions of the circular cylindrical shell can be derived as (Tzou, 1993; Tzou and Liu, 1997)

$$-\frac{\partial N_{xx}}{\partial x} - \frac{1}{R}\frac{\partial N_{x\beta}}{\partial \beta} + \rho h \ddot{u}_1 = F_1 + \frac{\partial N_{xx}^c}{\partial x}$$

$$
\begin{aligned}
&-\frac{\partial N_{x\beta}}{\partial x}-\frac{1}{R}\frac{\partial N_{\beta\beta}}{\partial \beta}-\frac{1}{R}\Big(-\frac{\partial M_{x\beta}}{\partial x}+\frac{1}{R}\frac{\partial M_{\beta\beta}}{\partial \beta}\Big)+\rho h\ddot{u}_2= \\
&=F_2+\frac{1}{R}\frac{\partial N^c_{\beta\beta}}{\partial \beta}+\frac{1}{R^2}\frac{\partial M^c_{\beta\beta}}{\partial \beta} \qquad (3.1)\\
&-\frac{\partial^2 M_{xx}}{\partial x^2}-\frac{2}{R}\frac{\partial^2 M_{x\beta}}{\partial x^2}-\frac{1}{R^2}\frac{\partial^2 M_{\beta\beta}}{\partial \beta^2}+\frac{N_{\beta\beta}}{R}+\rho h\ddot{u}_3= \\
&=F_3+\frac{\partial^2 M^c_{xx}}{\partial x^2}+\frac{1}{R^2}\frac{\partial^2 M^c_{\beta\beta}}{\partial \beta^2}-\frac{N^c_{\beta\beta}}{R}
\end{aligned}
$$

where N_{ij} and M_{ij} are the elastic forces and moments; N^c_{ij} and M^c_{ij} denote the opto-mechanical control forces and moments; ρ is the shell mass density; $\ddot{u}_j$ are the accelerations; and F_1, F_2, F_3 are the external excitations, respectively. The distributed control forces N^c_{ij} and moments M^c_{ij} induced by the micro-protodeformation are defined by (Heaviside) step functions

$$
\begin{aligned}
N^c_{ij}(t_j)&=[Y^o_p h^o d_{3i} E^o_{I\theta}(t_j)+h^o\lambda_I\theta(t_j)]U_s(x)U_s(\beta) \\
M^c_{ij}(t_j)&=\frac{h+h^o}{2}[Y^o_p h^o d_{3i} E^o_{I\theta}(t_j)+h^o\lambda_I\theta(t_j)]U_s(x)U_s(\beta)
\end{aligned} \qquad (3.2)
$$

where Y^o_p is Young's modulus of the opto-mechanical actuator; h^o is the actuator thickness; d_{3i} is the piezoelectric strain constant; $E^o_{I\theta}(t_j)$, and $\theta(t_j)$ are respectively the photovoltaic/pyroelectric voltage and the body temperature induced by the high-energy illumination at the time t_j; and λ_I is the thermal stress constant, as discussed previously. The double step function $U_s(\beta)$ (rectangular shape) is defined by the four-corner coordinates (x^*_1 to x^*_2 in the x direction and β^*_1 to β^*_2 in the β direction) of the opto-mechanical actuator patch laminated on the shell, see Figure 2

$$
\begin{aligned}
U_s(\alpha_i)&=u_s(\alpha_i-\alpha^*_{i1})-u_s(\alpha_i-\alpha^*_{i2}) \\
u_s(\alpha_i-\alpha^*_{ij})&=\begin{cases}1 & \text{when} \quad \alpha_i \geqslant \alpha^*_{ij}\\ 0 & \text{when} \quad \alpha_i<\alpha^*_{ij}\end{cases}
\end{aligned} \qquad (3.3)
$$

where $i,j=x$ or β.

4. Modal decomposition and independent modal control

It is assumed that the dynamic response induced by the external forces, moments, and/or initial conditions can be synthesized by the participating

mode shape functions. The amount of each modal participation in the total dynamic response is defined by a modal participation factor $\eta_k(t)$. Thus, the total dynamic response can be represented by the summation of all participating natural modes multiplied by their respective modal participation factors

$$u_i(\alpha_1, \alpha_2, t) = \sum_{m=1}^{\infty} \sum_{n=1}^{\infty} \eta_{mn}(t) U_{imn}(\alpha_1, \alpha_2) \qquad i = 1, 2, 3 \tag{4.1}$$

where $U_{imn}(\alpha_1, \alpha_2)$ is the mode shape function; mn denotes the mn-th mode; m and n denote the mode (half-wave) numbers in the longitudinal and circumferential directions, respectively. Substituting the modal expansion equation into the shell equations, integrating over the whole shell surface and applying the modal orthogonality, one can derive the mn-th modal equation

$$\ddot{\eta}_{mn} + 2\zeta_{mn}\omega_{mn}\dot{\eta}_{mn} + \omega_{mn}^2 \eta_{mn} = \widehat{F}_{mn} \tag{4.2}$$

where ω_{mn} is the mn-th natural frequency; ζ_{mn} is the mn-th modal damping ratio and $\zeta_{mn} = c/(2\rho h \omega_{mn})$; and c is the damping constant. When the external mechanical forces $F_1 = F_2 = F_3 = 0$, the distributed modal (control) force $\widehat{F}_{kmn}$ induced by the opto-mechanical actuator patch is defined as

$$\begin{aligned} \widehat{F}_{kmn} &= \frac{1}{\rho h N_{mn}} \int_{x_1^*}^{x_2^*} \int_{\beta_1^*}^{\beta_2^*} \Big[\frac{\partial N_{xx}^c}{\partial x} U_{xkmn} + \Big(\frac{1}{R} \frac{\partial N_{\beta\beta}^c}{\partial \beta} + \frac{1}{R^2} \frac{\partial M_{\beta\beta}^c}{\partial \beta} \Big) U_{\beta kmn} + \\ &+ \Big(\frac{\partial^2 M_{xx}^c}{\partial x^2} + \frac{1}{R^2} \frac{\partial^2 M_{\beta\beta}^c}{\partial \beta^2} - \frac{N_{\beta\beta}^c}{R} \Big) U_{3kmn} \Big] \, dx d\beta \\ N_{mn} &= \int_{\alpha_1} \int_{\alpha_2} \sum_{k=1}^{3} U_{kmn}^2 \, d\alpha_1 d\alpha_2 \end{aligned} \tag{4.3}$$

Detailed modal control forces/moments $\widehat{F}_{kmn}$ are defined by the control algorithms, i.e., the Lyapunov control and the proportional feedback control discussed next.

4.1. Lyapunov control

In this case, the control force is defined by signum functions and it is reflected in induced micro-control actions (i.e., photodeformation induced strains) and controlled by the light illuminations

$$\widehat{F}_{kmn} = \frac{Y_p^o h^o}{\rho h N_{mn}}\Big[-\frac{A_k S_{11}}{n} + \frac{B_k L S_{22}}{mR\pi} + \frac{LS_{22}}{mnR\pi} + (h+h^o)\Big(\frac{m\pi S_{11}}{2nL} + \\ + \frac{nLS_{22}}{mR\pi} + \frac{B_k L S_{22}}{mR^2\pi}\Big)\Big]\Big(\cos\frac{m\pi x_1^*}{L} - \cos\frac{m\pi x_2^*}{L}\Big)(\sin n\beta_1^* - \sin n\beta_2^*) \tag{4.4}$$

where A_k, B_k are the normalized modal amplitudes; cosine and sine functions define the actuator spatial properties; the strains S_{ij} are the induced control strains resulting from the photovoltaic electric field Eq. (2.3) and the temperature Eq. (2.4) are defined previously in Eqs (2.1) and (2.2). However, the light intensity $\mathrm{I}(t_j)$ is now regulated by an on/off signum function

$$I(t_j) = I(t_{j-1}) + \{\Lambda[\operatorname{sgn}\dot{\eta}_{kj} G \max|\dot{\eta}_{kj}|] - I(t_{j-1})\} \tag{4.5}$$

where Λ is the light intensity gain and G is the feedback gain.

4.2. Proportional feedback control

It is assumed that the micro-control force/moment generated by the optical actuator is proportional to the vibration velocity in the proportional velocity feedback control. The control effect is reflected in the light intensity control and the modal control force takes the same form as above; the light intensity, however, is defined by the proportional control algorithm

$$I(t_j) = \Lambda[G\dot{\eta}_{kj} - \widehat{F}_{k(j-1)}] \tag{4.6}$$

5. Micro-control actions: in-plane (membrane) and out-of-plane (bending) actuations

The overall control effectiveness is introduced by two micro-control actions: the membrane control forces and the control moments. Thus, the kmn-th modal control force is divided into two parts: the membrane control component $(\widehat{F}_{kmn})_{memb}$ and the control moment component $(\widehat{F}_{kmn})_{bend}$

$$(\widehat{F}_{kmn})_{memb} = \frac{1}{\rho h N_{mn}} \int_{x_1^*}^{x_2^*}\int_{\beta_1^*}^{\beta_2^*}\Big(\frac{\partial N_{xx}^c}{\partial x} U_{xkmn} + \frac{1}{R}\frac{\partial N_{\beta\beta}^c}{\partial \beta} U_{\beta xkmn} + \frac{N_{\beta\beta}^c}{R}\Big)\, dx d\beta = \\ = \Big[\frac{Y_p^o h^o}{\rho h N_{mn}}\Big(-\frac{A_k S_{11}}{n} + \frac{B_k L S_{22}}{mR\pi} - \frac{LS_{22}}{mnR\pi}\Big)\Big]\cdot \\ \cdot\Big(\cos\frac{m\pi x_1^*}{L} - \cos\frac{m\pi x_2^*}{L}\Big)(\sin n\pi\beta_1^* - \sin n\pi\beta_2^*) \tag{5.1}$$

$$(\widehat{F}_{kmn})_{bend} = \frac{1}{\rho h N_{mn}} \int_{x_1^*}^{x_2^*} \int_{\beta_1^*}^{\beta_2^*} \Big[\frac{1}{R^2} \frac{\partial M^c_{\beta\beta}}{\partial \beta} U_{\beta x kmn} + \\ + \Big(\frac{\partial^2 M^c_{xx}}{\partial x^2} + \frac{1}{R^2} \frac{\partial^2 M^c_{\beta\beta}}{\partial \beta^2} \Big) U_{3xkmn} \Big] \, dx d\beta = \\ = \frac{h + h^o}{\rho h N_{mn}} Y_p^o h^o \Big(-\frac{m\pi S_{11}}{2nL} + \frac{nLS_{22}}{mR\pi} - \frac{B_k L S_{22}}{mnR^2\pi} \Big) \cdot \\ \cdot \Big(\cos \frac{m\pi x_1^*}{L} - \cos \frac{m\pi x_2^*}{L} \Big) (\sin n\pi\beta_1^* - \sin n\pi\beta_2^*) \tag{5.2}$$

It is observed that the spatial distribution parts of these force components are identical. Thus, the modal force of the kmn-th mode can be simply represented as

$$\widehat{F}_{kmn} = (\widehat{F}_{kmn})_{memb} + (\widehat{F}_{kmn})_{bend} \tag{5.3}$$

As discussed previously, S_{11} and S_{22} are respectively the control strains in the x and β directions induced by the photodeformation process. The original process involves three strain components due to the photovoltaic effect, the pyroelectric effect, and the opto-thermoelasticity. For convenience, one can add all three induced fields as $\widehat{E}_j$ and define the induced micro-control actions (strains) S_{11} and S_{22} as

$$S_{11} = \widehat{d}_{11} \widehat{E}_j \qquad \text{and} \qquad S_{22} = \widehat{d}_{22} \widehat{E}_j \tag{5.4}$$

where $\widehat{d}_{ij}$ are the resultant opto-mechanical strain constants. Substituting strain expressions into the membrane and moment control effects yields

$$(\widehat{F}_{kmn})_{memb} = \Big[\frac{Y_p^o h^o E'_j}{\rho h N_{mn}} \Big(-\frac{A_k \widehat{d}_{11}}{n} + \frac{B_k L \widehat{d}_{22}}{mR\pi} - \frac{L\widehat{d}_{22}}{mnR\pi} \Big) \cdot \\ \cdot \Big(\cos \frac{m\pi x_1^*}{L} - \cos \frac{m\pi x_2^*}{L} \Big) (\sin n\pi\beta_1^* - \sin n\pi\beta_2^*) = (\widehat{F}_{kmn})_{memb} \widehat{E}_j \\ (\widehat{F}_{kmn})_{bend} = (h + h^o) \Big[\frac{Y_p^o h^o E'_j}{\rho h N_{mn}} \Big(-\frac{m\pi \widehat{d}_{11}}{2nL} + \frac{nL\widehat{d}_{22}}{mR\pi} - \frac{B_k L \widehat{d}_{22}}{mnR^2\pi} \Big) \cdot \\ \cdot \Big(\cos \frac{m\pi x_1^*}{L} - \cos \frac{m\pi x_2^*}{L} \Big) (\sin n\pi\beta_1^* - \sin n\pi\beta_2^*) = (\widehat{F}_{kmn})_{bend} \widehat{E}_j \tag{5.5}$$

$(\widehat{F}_{kmn})_{memb}$ and $(\widehat{F}_{kmn})_{bend}$ are the resultant micro-actions denoted as the *control coefficients* of the kmn-th mode, which respectively indicate the modal membrane and bending control effectiveness of the actuator. Again, k denotes the k-th component mode of the mn-th shell mode. Furthermore, the control coefficients include both the feedback effect and the spatial effect.

6. Micro-control sensitivity study

Based on the analysis presented previously, distributed vibration control originates from two major micro-actions: the in-plane membrane control action and the out-of-plane bending control action. Contribution of these two actions on the cylindrical shell is respectively evaluated in this section. Furthermore, since distributed control effectiveness depends on the spatial characteristics of distributed actuators, thus, sensitivity analysis of actuator locations and sizes (width and length) is also studied and compared. It is assumed that the reference opto-mechanical actuator ($30\,\text{cm}\times 10\pi/11$) is placed from 0.2 m to 0.5 m and from $-5\pi/11$ to $5\pi/11$. The selection of an odd size actuator is to assure the maximal controllability of low natural modes. Mathematical model based simulations of the displacement and temperature responses of the opto-mechanical actuator at various light intensities are compared well with the experimental data (Liu and Tzou, 1998; Fukuda et al., 1993).

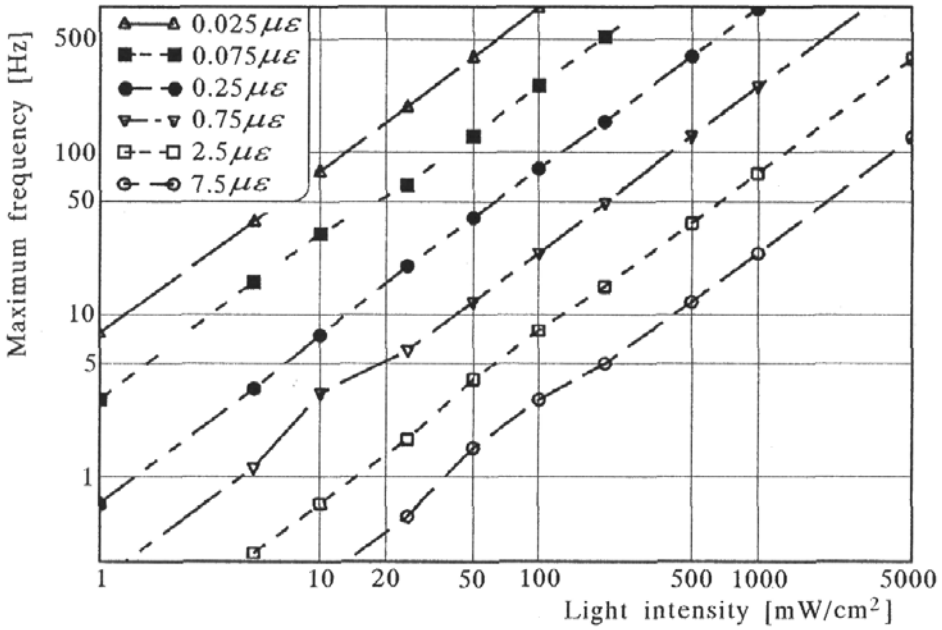

Fig. 3. Micro-actuation strain versus light intensity and actuation frequency

Detailed analytical and experimental comparisons are provided in Appendix. Note that the lines connecting modal data points presented in the following modal sensitivity figures only indicate the tendency, which are artificial because there is no mode between two mode-wave numbers. The line usually connects data points of one specific design parameter, such that these data are correlated. To evaluate the magnitude of control forces, the micro-actuation

(control) strain versus actuation frequency and light intensity is first calculated and plotted in Figure 3. It suggests that the actuation authority decreases when the actuation frequency increases at a given light intensity.

6.1. Micro-membrane and bending control effects

Micro-control actions denoted by *control coefficients*, $(\widehat{F}_{kmn})_{memb}$ of the membrane control forces and $(\widehat{F}_{kmn})_{bend}$ of the control moments of the $(m = 1,\ i = 1)$ mode of a thin cylinder $(h = 0.4\,\text{mm})$ are compared in Figure 4.

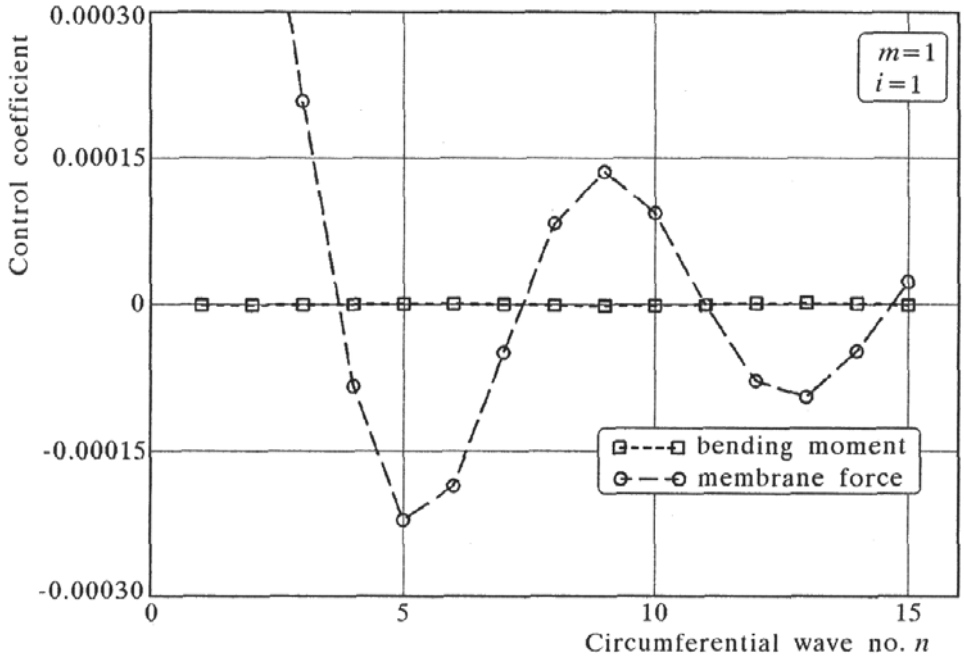

Fig. 4. Membrane and bending control actions of a thin cylindrical shell $(h = 0.4\,\text{mm})$

Control coefficients (modes $m = 1,\ i = 1$ and $m = 2,\ i = 1$) varying with respect to the mode number n for a thicker cylindrical shell $(h = 1\,\text{mm})$ are shown in Figure 5. Note that $i = 1$ denotes the transverse component mode of the three mode components, i.e., the transverse, circumferential, and longitudinal component modes. These results suggest that the control coefficients of membrane forces are much larger than those of control moments for most of modes $(n = 1, 2, ..., 15)$ and the absolute value decreases as the mode n increases. The bending control effect is relatively insignificant for lower natural modes. Variations are affected by the individual mode shape function and oscillation for the given opto-mechanical actuator patch. Summing the membrane control effect and the bending control effect gives the total modal

control effect. Note that the bending control effect is relatively insensitive as compared with the membrane control effect.

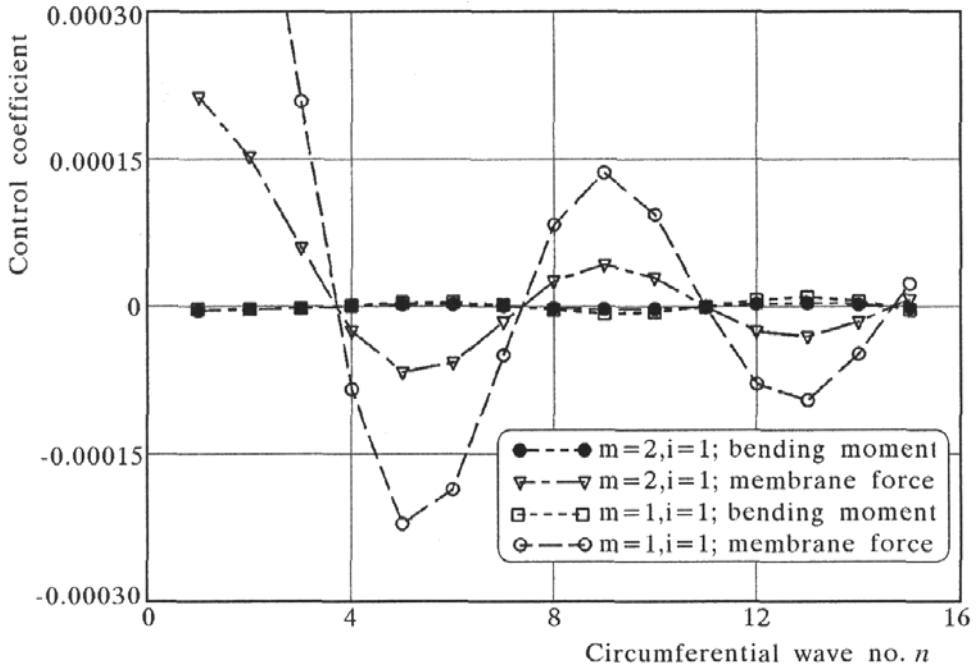

Fig. 5. Membrane and bending control actions of a thicker shell ($h = 1\,\text{mm}$)

Theoretical analysis reveals that the bending control effect increases as the moment arm increases. Accordingly, the bending control effect increases when the shell becomes thicker, only if the opto-mechanical actuator is surface laminated. Note that the membrane control effect remains identical as before. The control effect variations for the modes $m = 1$ and $m = 2$ are about the same, however, the $m = 2$ control effect is smaller than that of the $m = 1$ mode. As discussed previously, the variations depend on the individual mode shape function and oscillation for the specified opto-mechanical actuator patch (size and location). These factors are evaluated next.

6.2. Actuator length

It is assumed that the starting coordinate x_1^* is 0.2 m and the ending coordinate x_2^* changes (0.5, 0.6, 0.7, and 0.8 m), i.e., the actuator length changes. Micro-control actions (control coefficients) of the ($m = 1$, $n = 1, ..., 15$, $i = 1$) and ($m = 2$, $n = 1, ..., 15$, $i = 1$) modes are respectively plotted in Figures 6a,b. For the ($m = 1$, $n = 1, ..., 15$, $i = 1$) mode group, the control coefficients increase as the actuator becomes larger. The control coefficients for the ($m = 2$, $n = 1, ..., 15$, $i = 1$) mode group change from positive to ne-

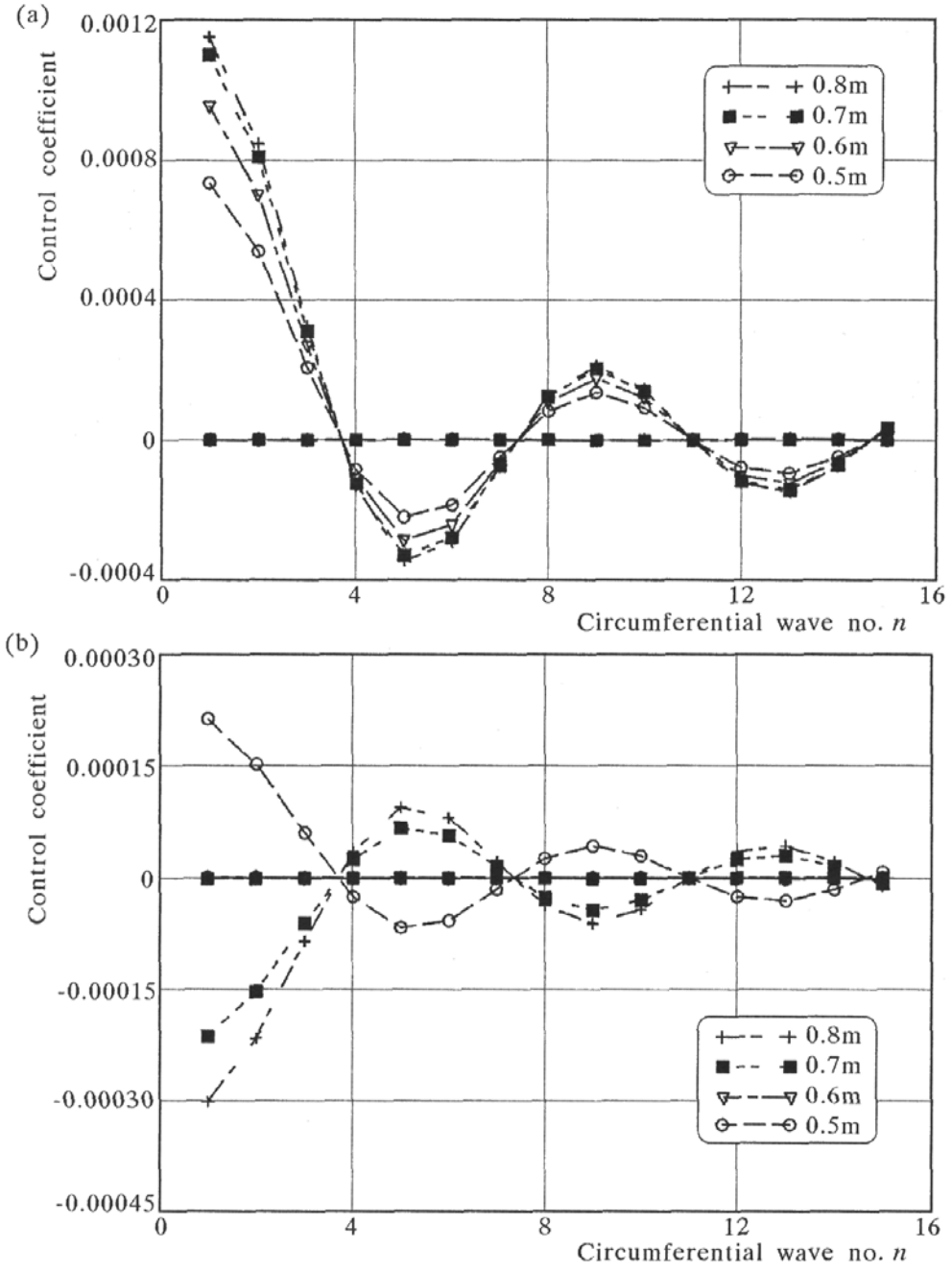

Fig. 6. Control actions for different actuator lengths; (a) $m = 1$, (b) $m = 2$

gative, due to the control strain cancellations and the mode shapes. Note that the symmetrically placed opto-mechanical actuator ($x_1^* = 0.2\,\mathrm{m}$, $x_2^* = 0.6\,\mathrm{m}$) does not have any control effect to all $m = 2$ modes. In this case, all control coefficients are zero, i.e., these modes are uncontrollable by the symmetrically placed opto-mechanical actuator.

6.3. Actuator width

Next, the actuator width $(\beta_2^* - \beta_1^*)$ in the circumferential direction is changed to $\pi/2$, $5\pi/4$, and $\pi/11$. Control coefficients of the two mode groups, i.e., $(m = 1,\ n = 1, ..., 15,\ i = 1)$ and $(m = 2,\ n = 1, ..., 15,\ i = 1)$, for the three actuator widths are respectively plotted in Figures 7a,b.

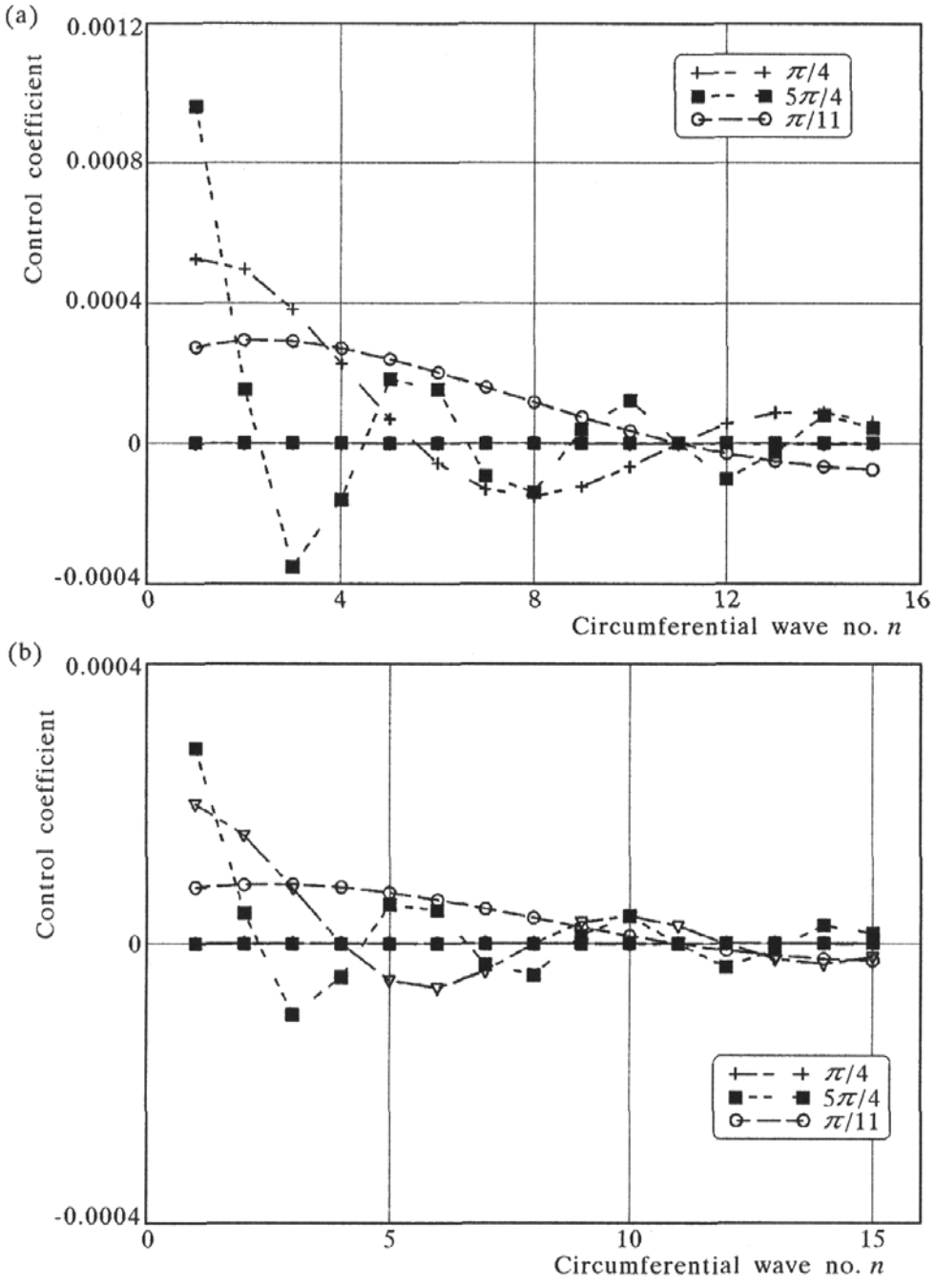

Fig. 7. Control actions for different actuator widths; (a) $m = 1$, (b) $m = 2$

It is observed that the wider opto-mechanical actuators give better control effects, however, the control coefficients also oscillate, as discussed previously. Also, it is noted that the symmetrical laminated actuator can not control quadruples of natural modes (i.e., $n = 4, 8, 12, ...$). The control coefficients decrease as the longitudinal mode number increases.

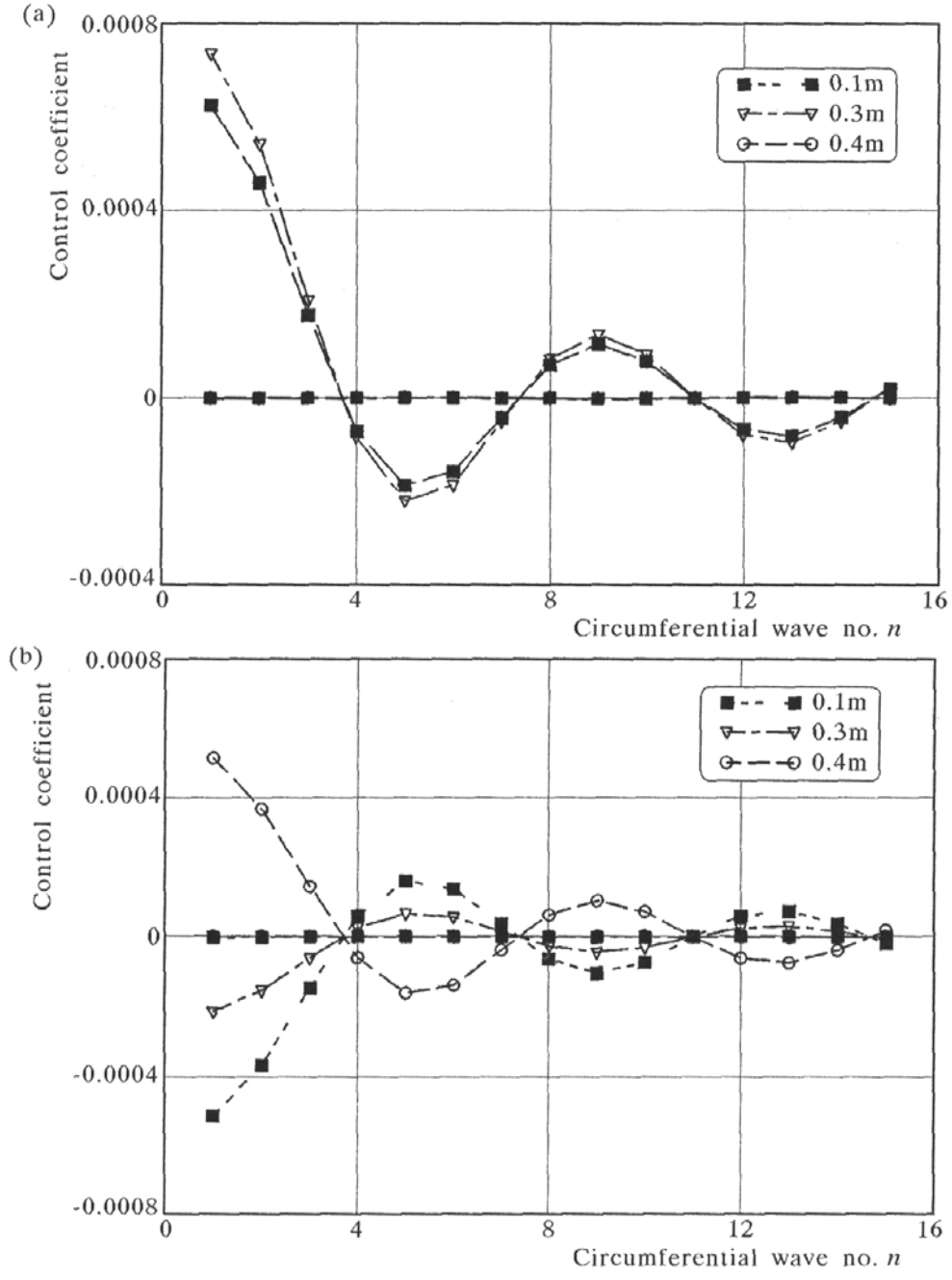

Fig. 8. Control actions for various actuator locations; (a) $m = 1$, (b) $m = 2$

6.4. Actuator location

Furthermore, a standard-size actuator ($30\,\text{cm} \times 10\pi/11$) is placed at various locations to investigate the location effects to control coefficients. The actuator moves in the length (longitudinal) direction and its starting coordinate x_1^* is used as a marking coordinate. Figures 8a,b respectively present the control coefficient variations of two mode groups ($m = 1$, $n = 1, ..., 15$, $i = 1$) and ($m = 2$, $n = 1, ..., 15$, $i = 1$) at three locations, i.e., $x_1 = 0.1\,\text{m}$, $0.3\,\text{m}$, and $0.4\,\text{m}$. Note that the control coefficients of the $x_1^* = 0.1\,\text{m}$ and $x_1^* = 0.4\,\text{m}$ are identical for the ($m = 1$, $n = 1, ..., 15$, $i = 1$) mode group, Figure 8a. This is because that these two locations are symmetrical respect to the shell center (i.e., the half-way). Also, the $x_1^* = 0.3\,\text{m}$ actuator leads to better control results, since this actuator is close to the middle location which is the optimal actuator location of the $m = 1$ mode. For the $m = 2$ mode group, there is a nodal line in the middle of the cylinder and the left and right sides oscillate in opposite directions. Thus, actuator locations greatly affect the micro-control actions, and thus, the overall control effects.

As demonstrated in this section, the modal controllability depends on the actuator sizes and locations. Accordingly, proper selection of actuator locations and sizes greatly influences the control effectiveness of the cylindrical shell.

6.5. Optimal actuator location

Optimal actuator locations, insensitive to the first six natural modes, are also calculated using the optimization procedures. The "dead zones" denoting the insensitive locations are illustrated in Figure 9. The horizontal axis denotes the circumferential direction (0 to 360 degrees) and the vertical axis denotes the longitudinal direction of a cylinder. In general, the actuators located in the dead zones are ineffective (or least effective) to the control of first six modes. Thus, effective sensor/actuator locations are outside these "dead zones", as noted in the figure.

6.6. Time history analysis

Actuator location/size and micro-membrane/bending control effects are investigated previously; transient time history responses with and without control are calculated and compared in this section. The controlled natural modes of the cylindrical shell are limited to lower natural modes. A velocity signal of a reference point obtained by the optimization procedure is used in the velocity feedback control – the proportional velocity feedback and the Lyapunov feedback. It is assumed that the opto-mechanical actuator is placed

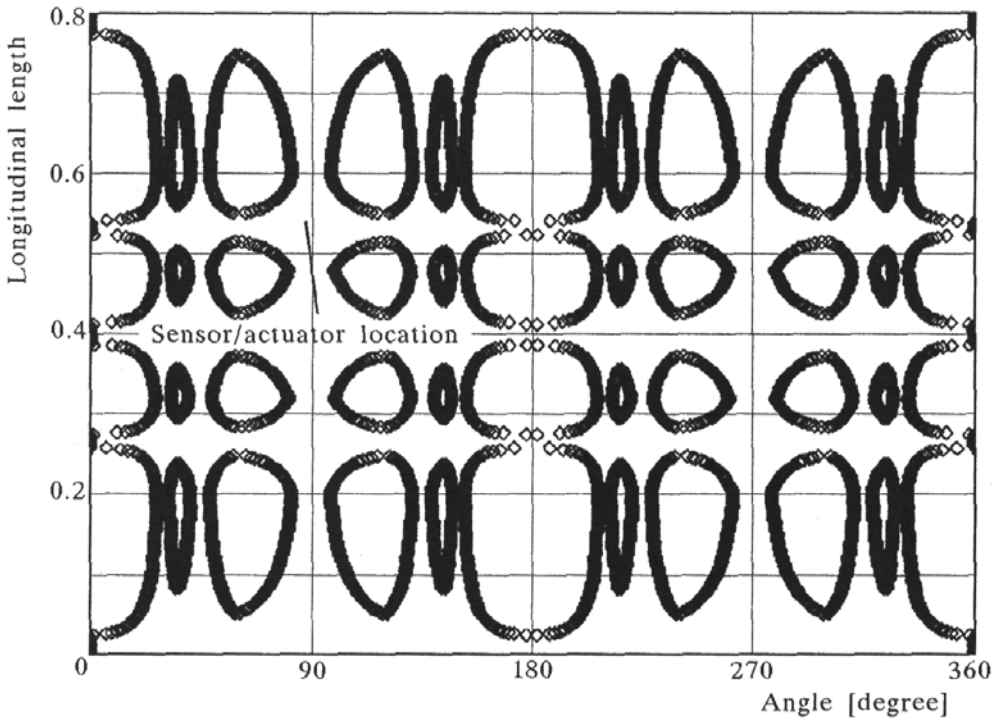

Fig. 9. Nodal zone of the first six modes ($m = 1, 2, 3$; $n = 1, 2, 3$) of the cylindrical shell

from 0.2 m to 0.5 m and from $-5\pi/11$ to $5\pi/11$. An initial displacement of 1.0×10^{-4} m is imposed and the snap back responses with and without control are investigated. Note that only the modal coordinate responses are plotted. The physical modal displacement response can be obtained by multiplying the modal response by the mode shape function. The resultant cylinder response is obtained by summing all participating modal responses. Transient time history responses of the cylindrical shell of the free oscillation and with the Lyapunov control and the negative velocity proportional feedback control are calculated and presented. For a demonstration purpose, two low natural modes, the (1,9) mode with the lowest frequency and an arbitrary (1,5) mode, are presented in Figures 10a,b.

Free response and control responses are compared in each figure. Note that the damped frequencies change due to the enhanced controlled damping ratios. Settling times of the time history responses can also be used to compare the control effectiveness. For example, the 10% settling times of the (1,5) mode corresponding to the proportional feedback control, the Lyapunov control and the free response are respectively 0.28 s, 0.10 s and 0.44 s. Apparently, the Lyapunov control provides a better control effect than that of the proportio-

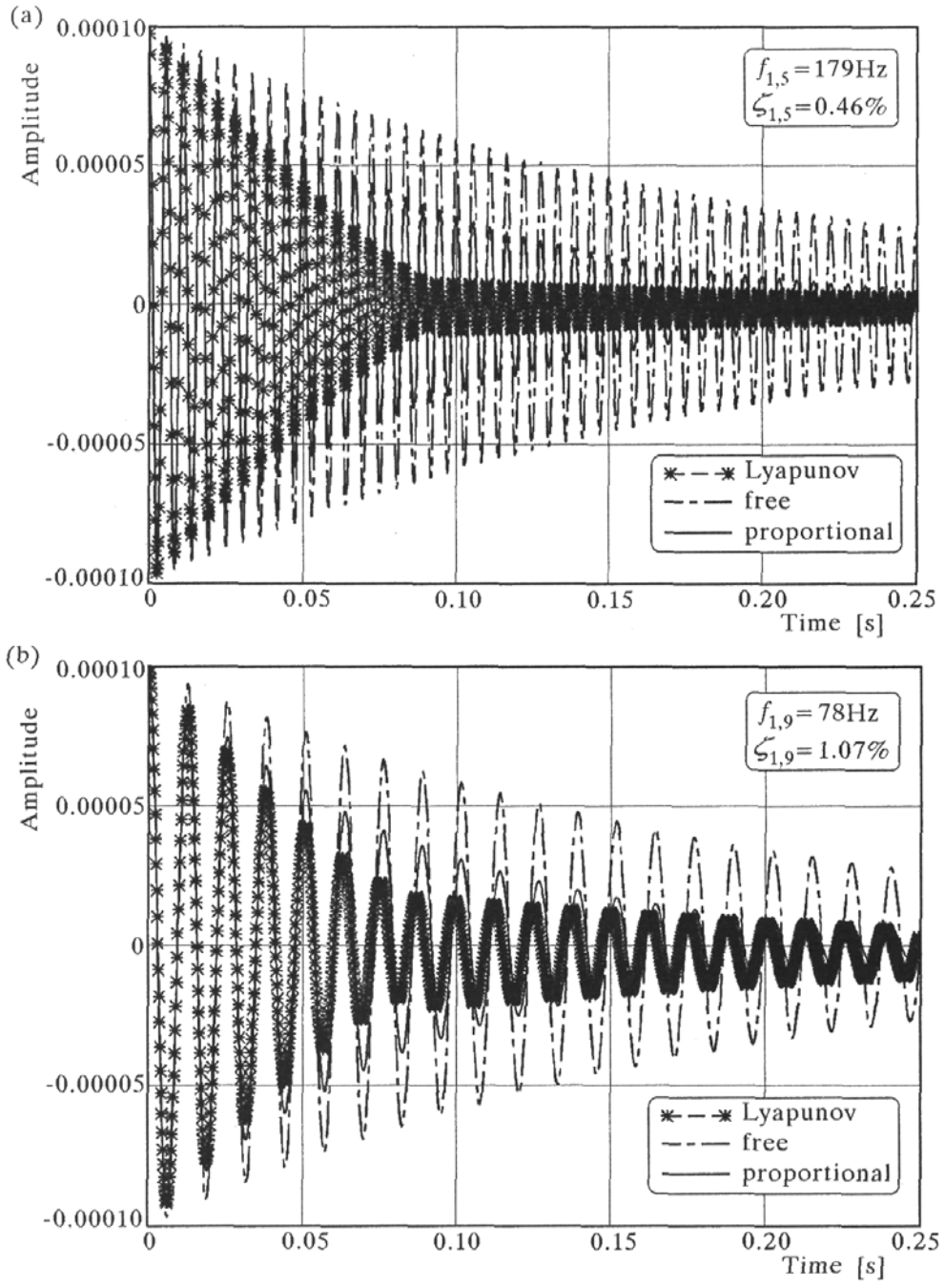

Fig. 10. Time histories of the free and controlled responses; (a) (1,5) mode, (b) (1,9) mode

nal control. (This behavior also complies with a number of earlier studies of distributed systems with piezoelectric actuators (Liu and Tzou, 1998; Tzou, 1993)).

7. Conclusions

Light-activated distributed opto-mechanical actuators represent a new class of distributed actuators offering non-contact distributed actuation without hard-wire connections. In general, a high-energy light first induces a charge/voltage generation based on the photovoltaic effect consequently introducing mechanical strains due to the converse piezoelectric effect. The photodeformation process involves both the photovoltaic effect and the converse piezoelectric effect. These induced photodeformations (strains) are carefully manipulated in the opto-mechanical actuators such that distributed micro-control actions can be applied to control of elastic structures. Modeling of a circular cylindrical shell laminated with distributed opto-mechanical actuator patches was presented and the closed-loop opto-piezo(electric)thermoelastic equations were derived. The system equations revealed the couplings among elasticity, photodeformation, pyroelectricity, and thermoelasticity. Solution procedures based on the modal analysis technique were outlined and the microscopic control mechanism of the opto-mechanical actuator patches was investigated. The resultant micro-control actions include 1) the membrane control effect and 2) the control moment effect in which the membrane control force contributes the in-plane control effect and the control moment counteracts the bending oscillations. Formulations of the proportional and the Lyapunov control algorithms were also presented.

Numerical simulations and sensitivity studies suggested that the distributed opto-mechanical actuators are effective for controlling low frequency modes. The resultant micro-control action can be divided into a membrane control action and a bending control action, and the former is effective to in-plane modes and the latter is effective to bending modes. Sensor/actuator placements and actuator sizes also dominated the control effectiveness of selected natural modes. Symmetrical layouts usually are ineffective to even modes or quadruple modes of a symmetrical structure. Time-history analyses illustrated the control effectiveness of the distributed opto-mechanical actuator and suggested that the Lyapunov control is more effective than the proportional control. Note that all results were based on theoretical analysis and numerical simulations with certain extrapolation of the present material properties based on available experimentally calibrated data. Further experiments or finite element analysis should be carried out to validate the results. Besides, the dynamic response of current experimental photostrictive materials is relatively slow and these materials are ineffective to high-frequency control.

Appendix: Comparisons between the mathematical model and experimental data

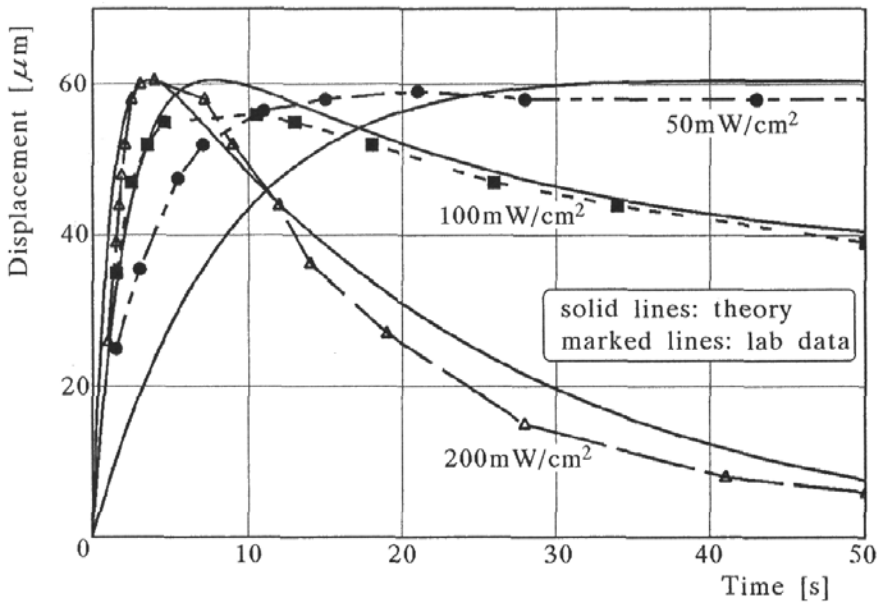

Fig. 11. Displacement responses at various illumination powers

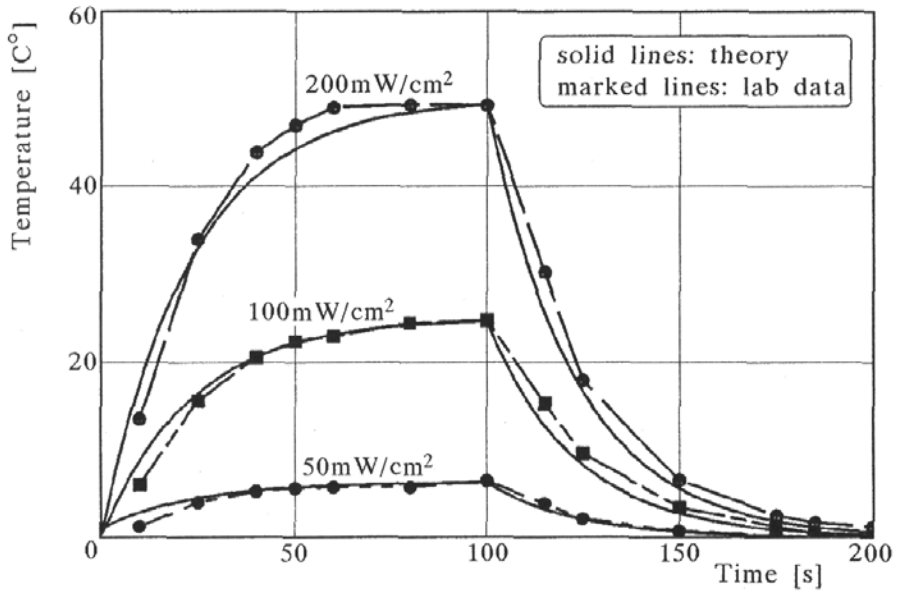

Fig. 12. Temperature responses at various illumination powers

References

1. BRODY P.S., 1983, Optomechanical bimorph actuator, *Ferroelectrics*, **50**, 27-32
2. FUKUDA T., HATTORI S., ARAI F., MATSUURA H., HIRAMATSU T., IKEDA Y., MAEKAWA A., 1993, Characteristics of optical actuator-servomechanisms using bimorph optical piezoelectric actuator, *Proceedings IEEE Robotics and Automation Conference*, Atlanta, May 1993, 618-623
3. LIU B., TZOU H.S., 1996, Photodeformation and light-temperature-electric coupling of optical actuators, Part-1: Parameter calibration, Part-2: Vibration control, *Proceedings of the ASME Aerospace Division*, AD-52, 663-678, *ASME 1996 International Congress*, Atlanta, GA, November 17-22
4. LIU B., TZOU H.S., 1998, Distributed photostrictive actuation and opto-piezothermoelasticity applied to vibration control of plates, *ASME Transactions, Journal of Vibration and Acoustics*, **120**, 937-943
5. MORIKAWA Y., NAKADA T., CAO D.H., 1993, Estimation of dynamic characteristics of bimorph type optical actuator and proposal of opto-pneumatic servo system, *Journal of Mechanical Engineering Laboratory* (Japanese), **47**, 237-246
6. SHIH H.-R., TZOU H.S., 2000, Opto-piezothermoelastic constitutive modeling of a new 2-D photostrictive composite plate actuator, *Proceedings of 2000 ASME International Mechanical Engineering Congress and Exposition*, **AD-61**, 1-8
7. SUSKI J., LARGEAU D., STEYER A., VAN DE POL F.C.M., BLOM F.R., 1990, Optically activated ZnO/SiO2/Si cantilever beams, *Sensors and Actuators*, **24**, 221-225
8. TZOU H.S., 1993, *Piezoelectric Shells: Distributed Sensing and Control of Continua*, Kluwer Academic Publishers, Dordrecht/Boston/London
9. TZOU H.S., BERGMAN L.A., EDITORS, 1998, *Dynamics and Control of Distributed Parameter Systems*, Cambridge University Press, New York, NY
10. TZOU H.S., CHOU C.-S., 1996, Nonlinear optoelectromechanics and photodeformation of optical actuators, *Journal of Smart Materials and Structures*, **5**, 230-235
11. TZOU H.S., FUKUDA T., EDITORS, 1992, *Precision Sensors, Actuators, and Systems*, Kluwer Academic Publishers, Dordrecht/Boston/London
12. TZOU H.S., LIU B., 1997, Light-induced non-contact actuation and control with photostrictive actuators, *Proceedings of DETC'97*, Paper No. DETC'97/Vib-3930, *ASME Design Engineering Technical Conferences*, September 14-17, Sacramento, California
13. TZOU H.S., YE R., 1994, Piezothermoelasticity and precision control of piezoelectric systems, *ASME Journal of Vibration and Acoustics*, **116**, 4, 489-495

Oddziaływania optopiezotermosprężyste i analiza wrażliwości mikrosterowania w optomechanicznych cylindrycznych powłokowych elementach wykonawczych

Streszczenie

Opto-mechaniczne elementy wykonawcze sterowane wysokoenergetycznym światłem reprezentują nową klasę bezstykowych precyzyjnych aktuatorów działających przy wykorzystaniu procesu fotodeformacji. Proces fotodeformacji opiera się na dwóch podstawowych zjawiskach sprzężenia opto-piezo(elektryczno)termosprężystego: 1) efektu fotowoltaicznego i 2) odwrotnego efektu piezoelektrycznego. Wysokoenergetyczne światła napromieniowujące takie, jak lasery lub ultrafiolet mogą zainicjować w pewnym typie materiałów fotostrykcyjnych proces fotodeformacji, który może być wykorzystany do bezstykowych elementów sterujących i wykonawczych o dużej precyzji. Indukowany temperaturowo efekt piroelektryczny, ujawniający się w procesie fotodeformacji oraz efekt odkształcenia termicznego wpływają na odpowiedź całego elementu. W pracy przedstawiono szacunkowe ujęcie wrażliwości mikrosterowania i efektywności przestrzennego rozkładu ciągłych opto-mechanicznych powłokowych elementów wykonawczych. W pierwszej części pracy przybliżono problem modelowania matematycznego powłoki cylindrycznej laminowanej razem z opto-mechanicznym aktuatorem. W części dalszej przedstawiono analityczne rozwiązania postawionego zagadnienia. Układ zbadano przy różnych parametrach konstrukcyjnych i oddziaływaniach mikrsterujących, np. przy modalnym sterowaniu drgań membranowych oraz giętnych i określono wpływ położenia aktuatorów oraz stosunku ich długości do rozmiaru układu. Zamieszczono przebiegi czasowe odpowiedzi układu bez i ze sterowaniem.

Manuscript received March 13, 2002; accepted for print April 4, 2002